ChemPubSoc Europe

DOI: 10.1002/open.201900236

Open Access ChemistryOPEN Full Papers

Influence of Calcination Conditions on Structural and Solid-State Kinetic Properties of Iron Oxidic Species Supported on SBA-15

Nina Sharmen Genz* and Thorsten Ressler*[a]

Iron oxidic species supported on silica SBA-15 were synthesized with various iron loadings using two different Fe^{III} precursors. The effect of varying powder layer thickness during calcination on structural and solid-state kinetic properties of Fe_xO_y/SBA-15 samples was investigated. Calcination was conducted in thin (0.3 cm) or thick (1.3 cm) powder layer. Structural characterization of resulting Fe_xO_y/SBA-15 samples was performed by nitrogen physisorption, X-ray diffraction, and DR-UV/Vis spectroscopy. Thick powder layer during calcination induced an increased species size independent of the precursor. However, a significantly more pronounced influence of calcination mode on species size was observed for the Fe^{III} nitrate precursor compared to the Fe^{III} citrate precursor. Temperature-programmed reduction (TPR) experiments revealed distinct differences in reducibility and reduction mechanism dependent on calcination mode. Thick layer calcination of the samples obtained from Fe^{III} nitrate precursor resulted in more pronounced changes in TPR profiles compared to samples obtained from Fe^{III} citrate precursor. TPR traces were analyzed by model-dependent Coats-Redfern method and model-independent Kissinger method. Differences in solid-state kinetic properties of Fe_xO_y/SBA-15 samples dependent on powder layer thickness during calcination correlated with differences in iron oxidic species size.

1. Introduction

In catalysis research, revealing reliable structure-activity correlations requires reducing chemical and structural complexity of metal oxide catalysts. Therefore, dispersing metal oxides on well-defined support materials has been shown to result in suitable model systems.[1] Ordered mesoporous silica materials, e.g. SBA-15 or MCM-41,[2,3] ordered mesoporous carbon, e.g. CMK-3,[4,5] and alumina oxides[6,7] are among the most commonly applied and investigated support materials. Moreover, MgO, TiO_2, ZrO_2 or zeolites are applied as high surface support materials in heterogeneous catalysis.[8–11] Supporting metal oxides on high surface materials can achieve highly dispersed and well-separated catalytically active sites. A further advantage is the higher thermal stability of particular metal oxide structures on support materials.[8,10,11] Dependent on the support material, metal oxides exhibit significant differences in electronical and chemical properties compared to bulk materials. Various synthesis procedures for dispersing active iron oxide species on suitable support materials have been described in the literature. However, it remains challenging to achieve well-dispersed and small or even isolated supported iron species.[12]

Catalytic activity of supported metal oxide catalysts is influenced particularly by support material properties such as acidity and pore structure,[1,9,13] size and dispersion of catalytically active sites,[4,6,12,14,15] metal precursor,[4,6,12,16,17] and calcination conditions.[7,18] Therefore, varying only selected parameters during synthesis appears preferable for deducing reliable structure-activity correlations.[1,4,18] Iron-containing catalysts are active in various reactions, such as Fischer-Tropsch synthesis, Friedel-Crafts alkylations, NO_x removal, and selective oxidation reactions.[4,7,17,19] Previously, investigations of iron-containing catalysts were reported regarding the correlation between iron species size, precursor and promotor effect, as well as calcination temperature and catalytic activity.[4,6,7,15,16,20] Al-Fatesh et al.[7] revealed a distinct effect of calcination temperature on catalytic activity of Fe/Al_2O_3 catalysts for catalytic methane decomposition (CMD). Fe/Al_2O_3 samples calcined at lower temperatures were reported to show higher reducibility and higher activity than samples calcined at higher temperature. Torres Galvis et al.[6] investigated the effect of precursors on catalytic performance of Fe/α-Al_2O_3 catalysts for Fischer-Tropsch synthesis of lower olefins (FTO). They showed an impact of the precursor on both dispersion of iron species and resulting iron species size. Significant precursor-dependent differences in catalytic activity resulted only from iron loadings of 5 wt% or 10 wt%. These differences in FTO selectivity were attributed to different aggregation of iron species. Influencing the dispersion of iron species of FeO_x/SiO_2 catalysts by various synthesis methods were reported by Arena et al.[15] and He et al.[14]. Arena et al.[15] showed an enhanced MPO (selective oxidation of methane to formaldehyde) performance for low-loaded FeO_x/

[a] N. S. Genz, Prof. Dr. T. Ressler
Institut für Chemie
Technische Universität Berlin
Straße des 17. Juni 135
10623 Berlin, Germany
E-mail: thorsten.ressler@tu-berlin.de
n.genz@tu-berlin.de

SiO_2 catalysts obtained by adsorption/precipitation method by improving the dispersion of active sites. The increased activity in MPO reported by He et al.[14] was also attributed to higher dispersion accompanied by higher amount of isolated iron species which was achieved by sol-gel synthesis. For supported copper oxide particles, an influence of calcination mode, i.e. thickness of powder layer during calcination, has been revealed by Koch et al.[18] They reported a distinct effect of thick layer calcination on size and electronic structure of copper oxides. Thick layer calcination was associated with an increased copper particle size compared to thin layer calcination and a decreased reducibility.

Investigations of structure-activity correlations in heterogeneous catalysis are frequently performed using time-resolved measurements under non-isothermal conditions. Hence, additional solid-state kinetic analysis of experimental data measured under these conditions may be helpful in corroborating correlations of structure and function of heterogeneous catalysts.[21] Applicability of solid-state kinetic analysis to supported iron species on mesoporous silica SBA-15 was recently reported.[17] The study showed that solid-state kinetic analysis can corroborate conventional characterization of supported systems. Here, the influence of varying powder layer thickness during calcination on structural and solid-state kinetic properties of supported iron oxidic species was investigated. In addition to conventional characterization, solid-state kinetic analysis was applied to elucidate correlations between iron loading, Fe^{III} precursor, calcination mode, and reducibility.

2. Results and Discussion

2.1. Sample Characterization

2.1.1. Nitrogen Physisorption Measurements

Surface properties and pore structure of Fe_xO_y/SBA-15_Th samples were determined from nitrogen physisorption measurements. Similar to SBA-15 support material, Fe_xO_y/SBA-15 samples obtained from thin layer calcination and thick layer calcination exhibited type IV nitrogen adsorption/desorption isotherms indicating mesoporous materials.[17,22,23] Figure 1 depicts physisorption isotherms of citrate_Th and nitrate_Th samples. Independent of the precursor, adsorption and desorption branches were nearly parallel at the hysteresis loop as expected for regularly shaped pores. Hysteresis loops of Fe_xO_y/SBA-15_Th samples were identified being of type H1 according to IUPAC.[23]

A decrease in specific surface area with increasing iron loading was recently reported for Fe_xO_y/SBA-15 samples obtained from thin layer calcination.[17] For citrate samples, specific surface area decreased from 725.2 to 605.7 m^2g^{-1} with increasing iron loading from 2.5 to 10.7 wt%, while for nitrate samples specific surface area decreased from 703.0 to 633.1 m^2g^{-1} with increasing iron loading from 2.0 to 9.3 wt%. Specific surface area of Fe_xO_y/SBA-15_Th samples decreased further compared to corresponding thin layer calcined samples

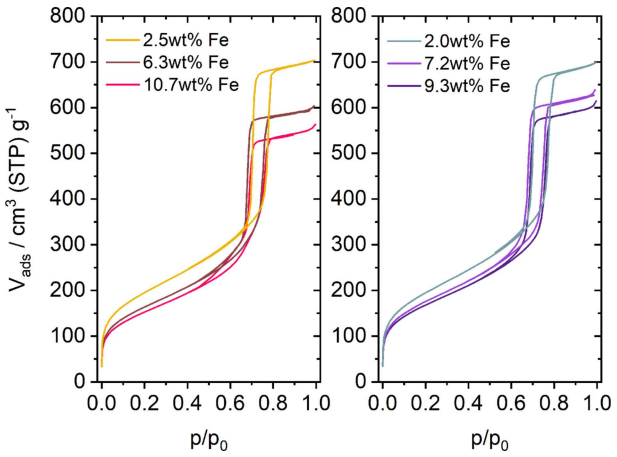

Figure 1. N_2 adsorption/desorption isotherms of Fe_xO_y/SBA-15_Th samples. Left: Citrate_Th samples. Right: Nitrate_Th samples

(Table 1). Pore size distributions were calculated by BJH method and revealed a narrow pore size distribution for all Fe_xO_y/SBA-15 samples independent of both precursor and calcination mode. Pore size distributions of Fe_xO_y/SBA-15_Th samples compared to corresponding thin layer calcined samples are depicted in Figure 2. The most pronounced influence of thick layer calcination was observed for the lowest loaded citrate and nitrate sample. Narrow pore size distribution of these samples was shifted to larger pore diameters after thick layer calcination. This shift amounted to 1.16 nm.

Additionally, pore volume, V_{pore}, was determined and summarized in Table 1. Thick layer calcination induced a decrease in pore volume compared to thin layer calcination. Conversely, 7.2 wt% Fe_Nitrate_Th and 9.3 wt% Fe_Nitrate_Th showed a slight increase in V_{pore}. For Fe_xO_y/SBA-15_Th samples, the decrease in specific surface area together with the decrease in pore volume with increasing iron loading indicated the presence of iron oxidic species in the mesopores of SBA-15.[20,22] Despite a slightly increased V_{pore}, indicating some mesopores might remain unfilled, iron oxidic species being mainly located in the mesopores of SBA-15 seemed also likely for 7.2 wt% Fe_Nitrate_Th and 9.3 wt% Fe_Nitrate_Th.

Table 1. Specific surface area, $a_{s,BET}$, and pore volume, V_{pore}, of Fe_xO_y/SBA-15_Th samples. Differences between Fe_xO_y/SBA-15_Th and corresponding Fe_xO_y/SBA-15 samples are denoted as Δ values.[a]

	$a_{s,BET}$/ m^2g^{-1}[b]	$\Delta a_{s,BET}$/ m^2g^{-1}	V_{pore}/ cm^3g^{-1}[c]	ΔV_{pore}/ cm^3g^{-1}
2.5 wt% Fe_Citrate_Th	700.0 ± 0.7	−25.5	1.087 ± 0.001	−0.025
6.3 wt% Fe_Citrate_Th	592.6 ± 0.6	−58.3	0.933 ± 0.001	−0.035
10.7 wt% Fe_Citrate_Th	550.2 ± 0.6	−55.5	0.865 ± 0.001	−0.033
2.0 wt% Fe_Nitrate_Th	701.7 ± 0.7	−1.3	1.079 ± 0.001	−0.017
7.2 wt% Fe_Nitrate_Th	633.4 ± 0.6	−14.4	0.987 ± 0.001	0.016
9.3 wt% Fe_Nitrate_Th	606.0 ± 0.7	−27.1	0.943 ± 0.001	0.004

[a] Measurement errors according to standard deviation determined from multiple measurements. [b] Specific surface area, $a_{s,BET}$, was calculated in the relative pressure range, p/p_0, of 0.05-0.26. [c] Pore volume, V_{pore}, is based on relative pressure, p/p_0, of 0.99.

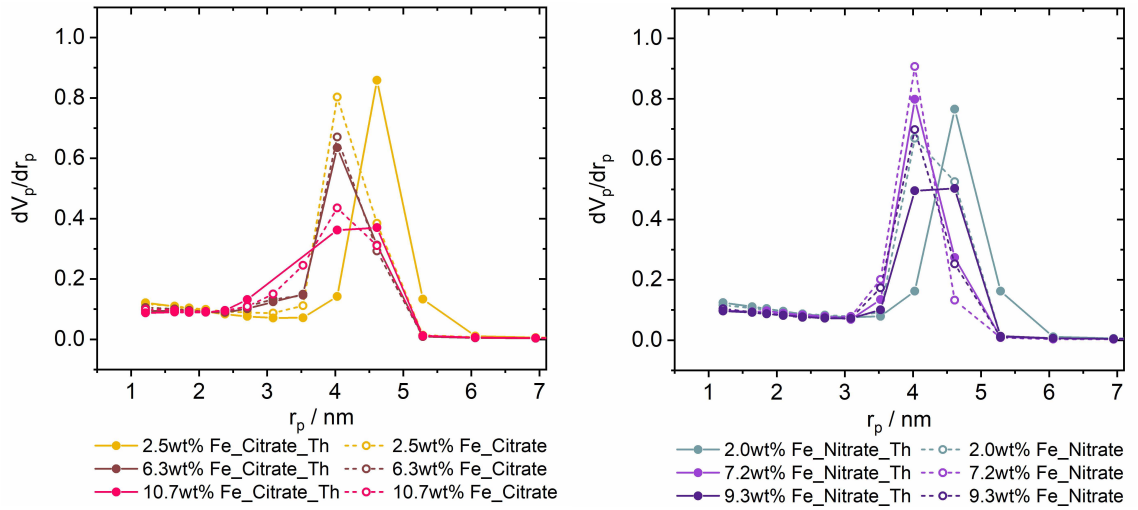

Figure 2. Left: Pore radius distribution of citrate_Th and corresponding citrate samples calculated by BJH method. Right: Pore radius distribution of nitrate_Th and corresponding nitrate samples calculated by BJH method.

Ratio of mesopore surface area, a_{pore}, calculated by BJH method[24] and specific surface area, $a_{s,BET}$, calculated by BET method,[25] was used for estimating the contribution of micropores to the entire surface area of SBA-15.[18,26] However, ratio of $a_{pore}/a_{s,BET}$ cannot be equated with an absolute value for the degree of micropore filling. Furthermore, the effect of powder layer thickness during calcination on ratio of $a_{pore}/a_{s,BET}$ was determined by calculating the difference between Fe_xO_y/SBA-15_Th and Fe_xO_y/SBA-15 samples (Table 2). Thick layer calcination induced an increased ratio of $a_{pore}/a_{s,BET}$, except for 2.0 wt% Fe_Nitrate_Th and 2.5 wt% Fe_Citrate_Th. These lowest loaded Fe_xO_y/SBA-15_Th samples possessed the same ratio of $a_{pore}/a_{s,BET}$, which was slightly decreased compared to that observed for corresponding Fe_xO_y/SBA-15 samples. Accordingly, thick layer calcination of lowest loaded samples correlated with an increased contribution of micropores to entire surface area, and hence, a lower degree of micropore filling. For iron loadings higher than 2.5 wt%, citrate_Th samples showed higher ratios of $a_{pore}/a_{s,BET}$ compared to nitrate_Th samples with similar iron loading. Apparently, using the citrate precursor resulted in stronger interactions between SBA-15 and Fe^{III} atoms of the precursor, and hence, in higher amounts of micropore filling, independent of layer thickness during calcination. This was ascribed to the more pronounced chelating effect the citrate precursor. Moreover, Fe_xO_y/SBA-15_Th samples showed a precursor-dependent trend in ratio of $a_{pore}/a_{s,BET}$ as function of iron loading. For citrate_Th samples, increasing the iron loading correlated with an increasing ratio of $a_{pore}/a_{s,BET}$. Conversely, for nitrate_Th samples, ratio of $a_{pore}/a_{s,BET}$ only increased up to 7.2 wt% iron, but decreased with further increasing iron loading. Influence of thick layer calcination on contribution of micropores to entire surface area was more pronounced for the citrate precursor.

Table 2. Contribution of micropores to entire surface area and surface roughness for Fe_xO_y/SBA-15_Th. Differences between Fe_xO_y/SBA-15_Th and corresponding Fe_xO_y/SBA-15 samples are denoted as Δ values.

	$a_{pore}/a_{s,BET}$ [a]	$\Delta(a_{pore}/a_{s,BET})$	ΔD_f [b]	$\Delta(\Delta D_f)$
2.5 wt% Fe_Citrate_Th	0.86	−0.02	−0.02 ± 0.02	−0.14
6.3 wt% Fe_Citrate_Th	0.94	0.05	0.32 ± 0.05	0.11
10.7 wt% Fe_Citrate_Th	0.95	0.04	0.41 ± 0.08	0.26
2.0 wt% Fe_Nitrate_Th	0.86	−0.02	0.02 ± 0.02	−0.04
7.2 wt% Fe_Nitrate_Th	0.90	0.02	0.20 ± 0.01	0.13
9.3 wt% Fe_Nitrate_Th	0.88	0.02	0.10 ± 0.02	0.16

[a] Ratio of mesopore surface area, a_{pore}, and specific surface area, $a_{s,BET}$, as measure of micropore contribution to the entire surface of SBA-15. [b] Differences in fractal dimension, ΔD_f, between SBA-15 and corresponding Fe_xO_y/SBA-15_Th samples as measure of the roughness of the surface.

In addition to BET and BJH method, modified FHH method was applied for analyzing nitrogen physisorption data of Fe_xO_y/SBA-15_Th samples. Resulting fractal dimension D_f was used as a measure of the roughness of the surface of SBA-15.[26,27] For Fe_xO_y/SBA-15 samples, as well as SBA-15, the fractal dimension was recently reported ranging between 2 and 3, indicating a rough surface of the support material.[17] ΔD_f values were calculated as difference between D_f values of SBA-15 and those of Fe_xO_y/SBA-15_Th samples for determining the influence of supported iron oxidic species on surface roughness of the support material (Table 2). In contrast to thin layer calcined Fe_xO_y/SBA-15 samples, thick layer calcined Fe_xO_y/SBA-15 samples possessed significantly higher differences in fractal dimension ΔD_f. Only for the lowest loaded nitrate and citrate sample ΔD_f values decreased due to thick layer calcination indicating an increased SBA-15 surface roughness (Table 2, Figure 3). This increased surface roughness complied with the decreased ratio of $a_{pore}/a_{s,BET}$. For iron loadings higher than 2.5 wt%, thick layer calcination induced significantly higher ΔD_f values compared to

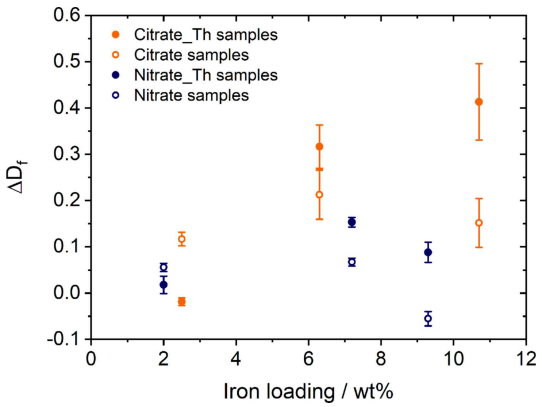

Figure 3. Differences in fractal dimension, ΔD_f, between SBA-15 support material and corresponding Fe_xO_y/SBA-15_Th and Fe_xO_y/SBA-15 samples, dependent on precursor and iron loading.

thin layer calcination, and hence, a smoother SBA-15 surface. A smoothing of SBA-15 surface for Fe_xO_y/SBA-15_Th samples agreed with an increased degree of micropore filling. This was induced by higher aggregated and less dispersed iron oxidic species of Fe_xO_y/SBA-15_Th samples. Moreover, compared to those of the nitrate_Th samples, the surface of SBA-15 of the citrate_Th samples were smoother. Whereas ΔD_f of the citrate_Th samples increased with increasing iron loading, those of the nitrate_Th samples increased up to 7.2 wt% iron and subsequently decreased for the highest loaded nitrate_Th sample (Table 2, Figure 3). This decrease in ΔD_f for 9.3 wt% Fe_Nitrate_Th was correlated with both significantly increased iron oxidic species size and increased amount of crystalline α-Fe_2O_3 for this sample (DR-UV/Vis, XRD). Such an increased iron oxidic species size agreed with the lowest pore volume for sample 9.3 wt% Fe_Nitrate_Th.

As reported for Fe_xO_y/SBA-15 samples obtained from thin layer calcination[17], precursor-dependent differences in surface roughness of the support material of Fe_xO_y/SBA-15_Th samples may be explained by different strengths of chelating effect of the two Fe^{III} precursors. However, thick layer calcination enhanced the aggregation and reduced the dispersion of iron oxidic species.

2.1.2. X-Ray Diffraction

Figure 4 depicts wide angle X-ray diffraction patterns of Fe_xO_y/SBA-15 samples for both calcination modes. For all Fe_xO_y/SBA-15_Th as well as for all Fe_xO_y/SBA-15 samples, a broad diffraction peak at 23° 2θ, was observed, corresponding to the amorphous silica structure of SBA-15.[14] XRD patterns of all citrate samples originating from either thin layer calcination or thick layer calcination, showed no further diffraction peaks. This was indicative of only small and highly dispersed iron oxidic species being present in citrate samples independent of powder layer thickness during calcination. XRD patterns of Fe_xO_y/SBA-15 samples originating from nitrate samples calcined in thin layer also showed no further diffraction peaks indicative of no long-range ordered phases. Conversely, XRD pattern of 9.3 wt% Fe_Nitrate_Th showed small diffraction peaks of crystalline α-Fe_2O_3. Furthermore, for 7.2 wt% Fe_Nitrate_Th, two main diffraction peaks of α-Fe_2O_3 were discernible, while 2.0 wt% Fe_Nitrate_Th showed no further diffraction peaks. Accordingly, using the nitrate precursor in thick layer calcination for iron loadings higher than 2.0 wt% induced significantly larger and less dispersed iron oxidic species on SBA-15 compared to those obtained from citrate precursor.

Small angle XRD patterns of Fe_xO_y/SBA-15_Th samples exhibited three characteristic diffraction peaks, (10 l), (11 l), and (20 l), corresponding to the two-dimensional hexagonal symmetry of SBA-15 (Figure 5).[2,28] Hence, as already reported for thin layer calcined Fe_xO_y/SBA-15 samples,[17] SBA-15 structure remained during synthesis with calcination in thick powder layer.

2.1.3. Diffuse Reflectance UV/Vis Spectroscopy

Figure 6 depicts DR-UV/Vis edge energies as function of iron loading of Fe_xO_y/SBA-15_Th samples, together with those of

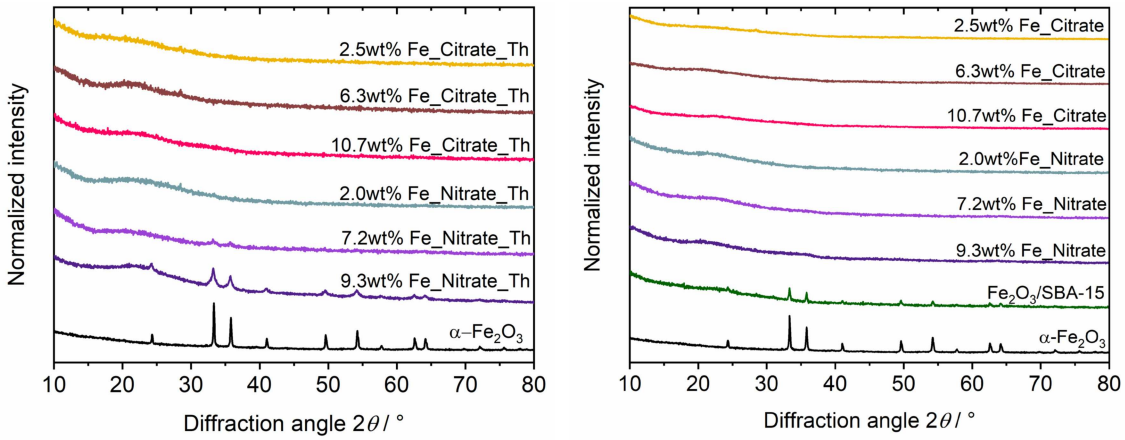

Figure 4. Left: Wide-angle X-ray diffraction patterns of Fe_xO_y/SBA-15_Th samples and crystalline α-Fe_2O_3. Right: Wide-angle X-ray diffraction patterns of Fe_xO_y/SBA-15 samples, the mechanical mixture, and crystalline α-Fe_2O_3.

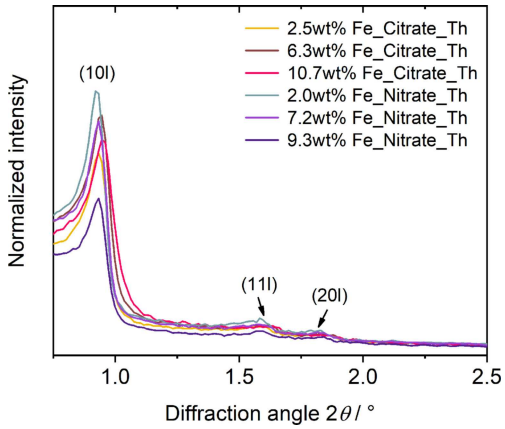

Figure 5. Small-angle X-ray diffraction patterns of Fe_xO_y/SBA-15_Th samples.

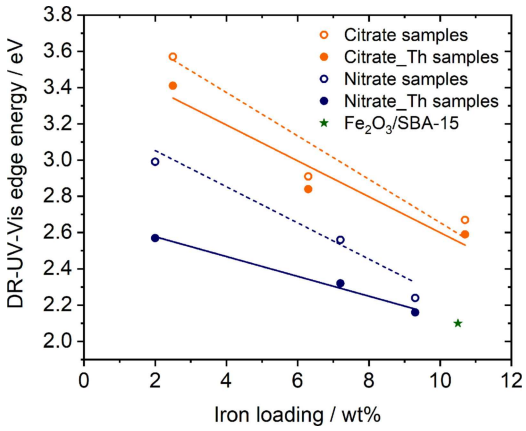

Figure 6. DR-UV/Vis edge energy of Fe_xO_y/SBA-15_Th, corresponding Fe_xO_y/SBA-15 samples, and the mechanical mixture Fe_2O_3/SBA-15 as function of iron loading. Error bars are smaller than the symbols.

corresponding Fe_xO_y/SBA-15 samples and that of the mechanical mixture, Fe_2O_3/SBA-15. Values of the DR-UV/Vis edge energy can be used for estimating relative metal oxide particle sizes. Both size and dispersion of transition metal oxides influence the position of the edge energy.[29] Edge energy values were determined from DR-UV/Vis spectra of Fe_xO_y/SBA-15_Th samples according to Weber[29]. All samples possessed edge energy values higher than that of crystalline α-Fe_2O_3 (2.10 eV), as observed for the mechanical mixture. Hence, for all Fe_xO_y/SBA-15_Th samples, iron oxidic species on SBA-15 were smaller than crystallites in α-Fe_2O_3 (average size of ~32 nm). Furthermore, edge energies of Fe_xO_y/SBA-15_Th samples were lower than 4.68 eV being the edge energy of isolated tetrahedrally coordinated Fe^{3+} in Fe-MFI zeolite (Si/Fe = 64).[30] As third reference, Fe^{III} nitrate precursor consisting of isolated octahedrally coordinated Fe^{3+} species was used and edge energy was determined to 3.53 eV. Except for 2.5 wt% Fe_Citrate_Th, all Fe_xO_y/SBA-15_Th samples possessed edge energy values lower than 3.53 eV. Thus, supported iron oxidic species were not only larger than isolated tetrahedrally coordinated Fe^{3+} species, but also larger than isolated octahedrally coordinated Fe^{3+} species, except for 2.5 wt% Fe_Citrate_Th.

A decrease in edge energy with increasing iron loading for all Fe_xO_y/SBA-15 samples independent of precursor and powder layer thickness during calcination correlated with an increasing iron oxidic species size. Furthermore, higher edge energies of citrate samples compared to those of nitrate samples for both calcination modes indicated smaller iron oxidic species resulting from citrate precursor. Comparing differences in edge energies between Fe_xO_y/SBA-15_Th and Fe_xO_y/SBA-15 samples revealed a more pronounced influence of powder layer thickness during calcination for the nitrate precursor. Additionally, decreasing iron loading correlated with an increasing difference in edge energy values between Fe_xO_y/SBA-15_Th and corresponding Fe_xO_y/SBA-15 sample. Hence, thick layer calcination induced a stronger increase in iron oxidic species size with decreasing iron loading. Independent of the precursor, thick layer calcination yielded higher aggregated and larger iron oxidic species on SBA-15 support material compared to thin layer calcination.

2.2. Correlation Between Fe_xO_y Species Size and Powder Layer Thickness During Calcination

Fe_xO_y species size of all Fe_xO_y/SBA-15 samples was increased after thick layer calcination. During thick layer calcination, retention time of gaseous decomposition products of the Fe^{III} precursors was extended compared to thin layer calcination. Accordingly, a higher concentration of these gaseous decomposition products in the powder layer resulted during calcination. Due to this higher concentration of gaseous decomposition products of the precursors, gas phase during calcination became relevant. Conversely, for thin layer calcination, influence of changing gas phase was negligible due to the fast removal of gaseous decomposition products of the precursors. Moreover, the effect of powder layer thickness during calcination on Fe_xO_y/SBA-15 samples was dependent on the precursor. The nitrate precursor induced a more pronounced Fe_xO_y species growth during thick layer calcination compared to the citrate precursor. In principle, three effects, i.e. composition of the gas phase, concentration of gaseous decomposition products, and dispersion of the Fe^{III} ions, might be relevant during thick layer calcination for precursor-dependent differences in resulting iron oxidic species size. In the following, it will be evaluated which of these three effects was decisive for the precursor-dependent differences in Fe_xO_y species size of Fe_xO_y/SBA-15_Th samples.

As first effect, the composition of the gas atmosphere might influence the Fe_xO_y species growth. For the nitrate precursor, Fe^{III} nitrate nonahydrate, thermal decomposition during calcination yielded nitrogen oxides and H_2O as gaseous decomposition products (Eq. (1),[31]). Conversely, thermal decomposition of the citrate precursor, (NH_4, Fe^{III}) citrate, resulted in nitrogen oxides, H_2O, and CO_2 as gaseous decomposition products (Eq. (2),).[31] For both precursors, nitrogen oxides and H_2O were observed. Therefore, these same gaseous decomposition products cannot induce the precursor-dependent differences in iron oxidic species size. Consequently, CO_2 was the only difference in gas phase composition. Hence, only CO_2 could induce the smaller and less aggregated Fe_xO_y species of the citrate_Th samples.

However, it appeared more reasonable that another effect significantly influenced iron oxidic species growth. Nevertheless, a possible influence of different compositions of the gas atmosphere on resulting iron oxidic species could not be excluded.

$$Fe(NO_3)_3 \cdot 9H_2O\ (s) \rightarrow Fe(NO_3)_3 \cdot 3H_2O\ (s) + 6\ H_2O\ (g) \rightarrow 0.5\ \alpha\text{-}Fe_2O_3\ (s) + 3\ H_2O\ (g) + 3\ NO_x\ (g) \quad (1)$$

$$[NH_4^+]_x\ [Fe^{3+}]_y\ [C_6H_5O_7^{3-}]\ (s) \rightarrow 0.5\ \alpha\text{-}Fe_2O_3\ (s) + 4.5\ H_2O\ (g) + NO_x\ (g) + 6\ CO_2\ (g) \quad (2)$$

As second effect, the concentration of gaseous decomposition products, and consequently a shift of the equilibrium during thermal decomposition of the precursors, was considered. Thermal decomposition of the precursors during calcination in thick powder layer may be described as heterogeneous equilibrium reaction. The extended retention time of the gaseous decomposition products during thick layer calcination shifted the equilibrium to the side of the educts, according to Le Chatelier's principle. This induced an increased decomposition temperature, and consequently, enhanced iron oxidic species growth and agglomeration. Compared to the nitrate precursor, thermal decomposition of the citrate precursor yielded higher concentrations of gaseous decomposition products (Eq. (1) and Eq. (2)). Accordingly, thick layer calcination of citrate samples induced a more pronounced shift of the equilibrium to the side of the educts. Therefore, a more pronounced iron oxidic species growth would be expected for the citrate samples compared to the nitrate samples. However, this was not observed. Quite the opposite, the nitrate precursor induced a more pronounced Fe_xO_y species growth during thick layer calcination compared to the citrate precursor. Hence, an effect of the concentration of gaseous decomposition products cannot induce the precursor-dependent differences in Fe_xO_y species size. However, the increased Fe_xO_y species size of all Fe_xO_y/SBA-15 samples due to thick layer calcination can be explained based on this effect.

As third effect, the dispersion of the Fe^{III} ions was considered. A higher dispersion of Fe^{III} ions hindered Fe_xO_y species growth. Due to the different strengths of chelating effect of the two precursors[17], dispersion of Fe^{III} ions varied dependent on the precursor. The citrate precursor possessing a more pronounced chelating effect, induced higher dispersed and encapsulated Fe^{III} ions before calcination. Therefore, Fe^{III} ions of the citrate precursor were too far away from each other which hindered aggregation during thick layer calcination. Accordingly, Fe_xO_y species growth and aggregation of citrate_Th samples was less pronounced compared to that of nitrate_Th samples. Apparently, this effect was stronger than that of the concentration of gaseous decomposition products during thermal decomposition of the precursors. Hence, the dispersion of the Fe^{III} ions was decisive for the precursor-dependent differences in Fe_xO_y species size of Fe_xO_y/SBA-15_Th samples.

Besides Fe^{III} precursor, iron loading affected the influence of powder layer thickness during calcination on resulting iron oxidic species. Independent of the precursor, lowest loaded Fe_xO_y/SBA-15_Th samples showed the most increased iron oxidic species size compared to corresponding Fe_xO_y/SBA-15 samples. This iron loading-dependent influence on Fe_xO_y species growth and aggregation was surprising. Since all above described effects were precursor-dependent, none of them could be assigned to the most increased Fe_xO_y species size of lowest loaded Fe_xO_y/SBA-15_Th samples. Apparently, the extended retention time of gaseous decomposition products was more influential for low iron loadings up to 2.5 wt%. A possible explanation might be a dependence of the retention time of gaseous decomposition products during calcination on the amount of precursor molecules, and therefore, on iron loading. At low amounts of precursor molecules, retention time was significantly shorter compared to that for higher amounts of precursor molecules. The difference in retention time of gaseous decomposition products between thick and thin layer calcination was presumably higher for low amounts of precursor molecules. Consequently, a more enhanced iron oxidic species growth resulted for lowest loaded Fe_xO_y/SBA-15_Th samples.

2.3. Reducibility of Fe_xO_y/SBA-15_Th Samples

TPR traces of Fe_xO_y/SBA-15_Th samples measured during reduction with H_2 at a heating rate of 10 K/min are depicted in Figures 7 and 8. Differences in reduction profiles of citrate_Th compared to citrate samples were only minor (Figure 7). Lowest loaded citrate_Th sample possessed one single reduction peak indicating a single-step reduction mechanism. The reduction peak of this citrate_Th sample was slightly broadened compared to that of the citrate sample. Higher loaded citrate_Th samples showed a two-step reduction mechanism (Figure 7, left). For all citrate_Th samples, a slight shift of the first TPR maximum towards lower temperatures compared to corresponding citrate samples was observed. This shift of the first TPR maximum indicated a better reducibility of the citrate samples obtained by thick layer calcination. According to literature,[14,15,22] reduction of isolated Fe^{3+} sites supported on mesoporous SiO_2 occurs at higher temperatures than reduction of Fe_xO_y oligomers (e.g. TPR maximum centered at 780 K for a sample with 0.05 wt% iron loading consisting mainly of isolated Fe^{3+} sites was shifted to 640 K as iron loading rose to 0.08 wt% and amount of Fe_xO_y oligomers increased). Therefore, improved reducibility of citrate_Th samples was attributed to higher amounts of Fe_xO_y oligomers as well as higher aggregated iron oxidic species induced by thick layer calcination.

In contrast to citrate_Th, nitrate_Th samples showed a more pronounced influence of powder layer thickness during calcination on reduction mechanism. TPR traces of nitrate_Th samples are depicted in Figure 8, left. While lowest loaded nitrate sample possessed a single-step reduction mechanism (Figure 8, right), corresponding nitrate_Th sample possessed a two-step reduction mechanism. Thick layer calcination of the higher

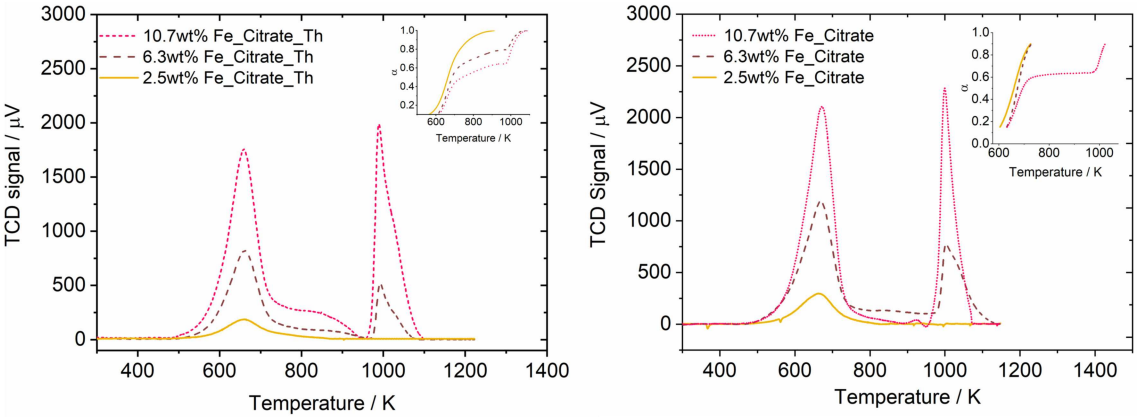

Figure 7. Left: TPR traces citrate_Th samples measured in 5% H_2 in 95% argon at 10 K/min. Inset depicts reduction degree traces with increasing iron loading from left to right. Right: TPR traces citrate samples measured in 5% H_2 in 95% argon at 10 K/min. Inset depicts reduction degree traces with increasing iron loading from left to right.

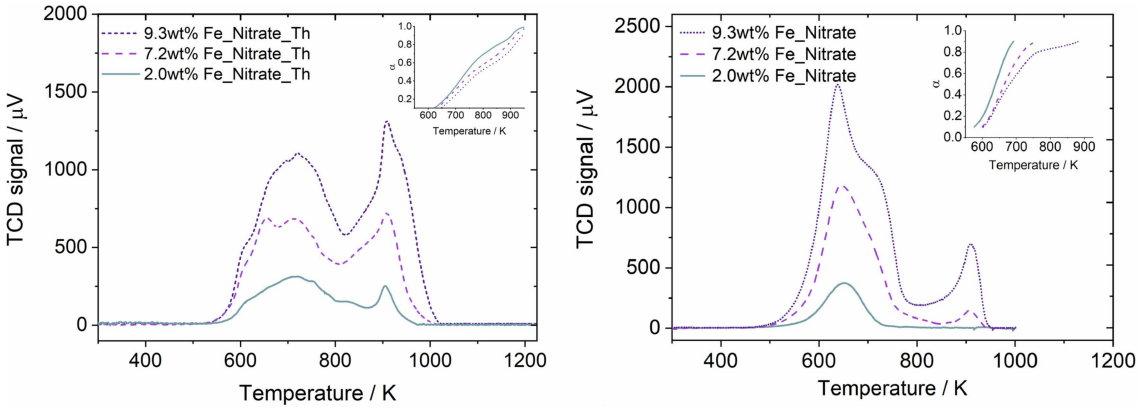

Figure 8. Left: TPR traces nitrate_Th samples measured in 5% H_2 in 95% argon at 10 K/min. Inset depicts reduction degree traces with increasing iron loading from left to right. Right: TPR traces nitrate samples measured in 5% H_2 in 95% argon at 10 K/min. Inset depicts reduction degree traces with increasing iron loading from left to right.

loaded nitrate samples also induced an increasing complexity of the reduction mechanism. TPR traces of 7.2 wt% Fe_Nitrate_Th and 9.3 wt% Fe_Nitrate_Th showed a multi-step reduction mechanism with less resolved reduction peaks in the lower temperature range. For nitrate_Th samples, a shift of the first TPR maximum to higher temperatures was observed. Interestingly, thick layer calcination of nitrate samples induced an opposite trend compared to that observed for thin layer calcination. For nitrate samples obtained from thin layer calcination, a better reducibility was observed with increasing iron loading[17] and therefore increasing amount of Fe_xO_y oligomers.[14,15,22] Conversely, the shift of the TPR maxima to higher temperatures for the nitrate_Th samples (Figure 8) indicated a better reducibility of less aggregated iron species. This shift of the first TPR maximum for the nitrate_Th samples was probably induced by an increasing amount of crystalline α-Fe_2O_3 with increasing iron loading. For crystalline α-Fe_2O_3, increasing particle size correlates with a hindered reducibility.[14,15,32] In addition to the shift of the TPR maxima, a significant broadening of the first reduction peak for nitrate_Th samples was observed. This broadening was attributed to both broadened size distribution of iron oxidic species and bulk diffusion limitation due to higher amounts of crystalline α-Fe_2O_3.[14] This coincided with the increasing iron species size (Figure 6) and increasing amount of α-Fe_2O_3 giving rise to X-ray diffraction peaks (Figure 4) with increasing iron loading of the nitrate_Th samples. Moreover, the shift of the TPR maxima induced by thick layer calcination mode compared to thin layer calcination mode was larger for nitrate samples than for citrate samples. This lager shift of the TPR maxima also indicated a more distinct effect of powder layer thickness during calcination on Fe_xO_y/SBA-15 samples obtained from Fe^{III} nitrate precursor.

2.4. Reduction Kinetics under Non-Isothermal Conditions

As previously reported[17], solid-state kinetic analysis can be successfully applied to supported systems and, therefore, constitutes an additional analysis method to obtain information on supported species. Prior to applying model-independent and model-dependent solid-state kinetic analysis methods, reduction degree α traces were extracted by integration of TPR

traces of all Fe_xO_y/SBA-15_Th samples. Resulted α traces are depicted in the inset in Figure 7 and Figure 8 for citrate_Th and nitrate_Th samples, respectively.

2.4.1. Kissinger Method

Model-independent Kissinger method yields a single apparent activation energy (E_a) of rate-determining step during reduction of Fe_xO_y/SBA-15_Th samples. By depicting $ln[\beta/T_m^2]$ as function of $1/T_m$, apparent activation energy of the reduction of Fe_xO_y/SBA-15_Th was calculated from the slope of the resulting straight line.[17,33,34] In order to enable comparison of E_a for all samples despite differing TPR traces, T_m corresponded to the first maximum of the TPR traces (Figures 7–8).

Apparent activation energies for Fe_xO_y/SBA-15_Th samples, corresponding Fe_xO_y/SBA-15 samples, and the mechanical mixture are summarized in Table 3. As already observed for Fe_xO_y/SBA-15, Fe^{III} precursor significantly influenced reducibility, and hence, apparent activation energy of rate-determining step in reduction of Fe_xO_y/SBA-15_Th samples.[17] Highest apparent activation energy of rate-determining step in reduction resulted for lowest loaded nitrate_Th sample. Increasing iron loading within the nitrate_Th samples correlated with a decreasing apparent activation energy of reduction. A correlation between increasing iron loading, i.e. increasing species size, and decreasing E_a, i.e. better reducibility, was already reported for nitrate samples obtained by thin layer calcination.[17] Higher loaded nitrate_Th samples, 7.2 wt% Fe_Nitrate_Th and 9.3 wt% Fe_Nitrate_Th, exhibited the same value of E_a within experimental errors as the mechanical mixture of α-Fe_2O_3 and SBA-15. This might be indicative of a similar size of iron oxidic species. Similarities in iron oxidic species size were corroborated by results from DR-UV/Vis spectroscopy and XRD. 7.2 wt% Fe_Nitrate_Th and 9.3 wt% Fe_Nitrate_Th possessed a DR-UV/Vis edge energy of 2.3 respectively 2.2 eV, being similar to that of Fe_2O_3/SBA-15 (2.1 eV) (Figure 6). Furthermore, these samples showed XRD peaks corresponding to crystalline α-Fe_2O_3 (Figure 4). Accordingly, increasing amount of crystalline α-Fe_2O_3 agreed with the decrease in E_a for higher loaded nitrate_Th samples. The highest apparent activation energy of 2.0 wt% Fe_Nitrate_Th coincided with the most distinct broadening of the first TPR peak (Figure 8). Thick layer calcination of the lowest loaded nitrate sample affected the most pronounced difference in iron oxidic species size. For this sample, increased species size, broadened species size distribution, and hence, increased complexity of the reduction mechanism were observed. Conversely, using the citrate precursor in thick layer calcination yielded highest apparent activation energy in reduction for highest loaded samples, while lowest loaded citrate_Th sample possessed lowest E_a. Furthermore, values of E_a for citrate_Th samples were higher compared to those of nitrate_Th samples for iron loadings higher than 2.5 wt%. This was indicative of a precursor-dependent trend in apparent activation energy as function of iron loading for Fe_xO_y/SBA-15_Th samples, as already observed for Fe_xO_y/SBA-15.[17]

For lowest loaded Fe_xO_y/SBA-15_Th samples, the most pronounced influence of powder layer thickness during calcination on apparent activation energy in reduction was observed (Figure 9). A significant increase in apparent activation energy of the reduction of 2.5 wt% Fe_Citrate_Th and 2.0 wt% Fe_Nitrate_Th, compared to corresponding Fe_xO_y/SBA-15 samples, was observed. This might be induced by a broadened species size distribution, being reflected in the broadening of the first TPR maxima. Accordingly, reduction of iron oxidic species with different sizes, ascribed to the first TPR peak, was more difficult compared to that of iron oxidic species with a narrow species size distribution. This yielded an increased apparent activation energy.

Table 3. Apparent activation energy, E_a, of rate-determining step in reduction of Fe_xO_y/SBA-15_Th, corresponding Fe_xO_y/SBA-15 samples, and the mechanical mixture Fe_2O_3/SBA-15. [a]

	Ea / kJ/mol	
	Thick layer calcined	Thin layer calcined
2.5 wt% Fe_Citrate	76±7	39±8
6.3 wt% Fe_Citrate	102±8	113±8
10.7 wt% Fe_Citrate	88±8	104±8
2.0 wt% Fe_Nitrate	130±3	88±8
7.2 wt% Fe_Nitrate	69±5	84±1
9.3 wt% Fe_Nitrate	70±5	62±8
Fe_2O_3/SBA-15	59±7	

[a] E_a values were determined by Kissinger method and reduction was conducted in 5% H_2 in argon.

2.4.2. Coats-Redfern Method

Model-dependent Coats-Redfern analysis[34,35] was applied for providing a complementary analysis method of the non-isothermal kinetic data.

The Coats-Redfern method is based on:

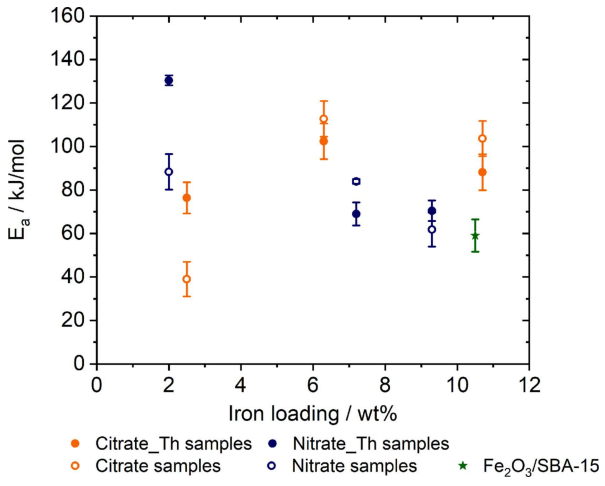

Figure 9. Apparent activation energy, E_a, of rate-determining step in reduction (5% H_2 in argon) determined by Kissinger method for Fe_xO_y/SBA-15_Th, corresponding Fe_xO_y/SBA-15 samples, and the mechanical mixture as function of iron loading.

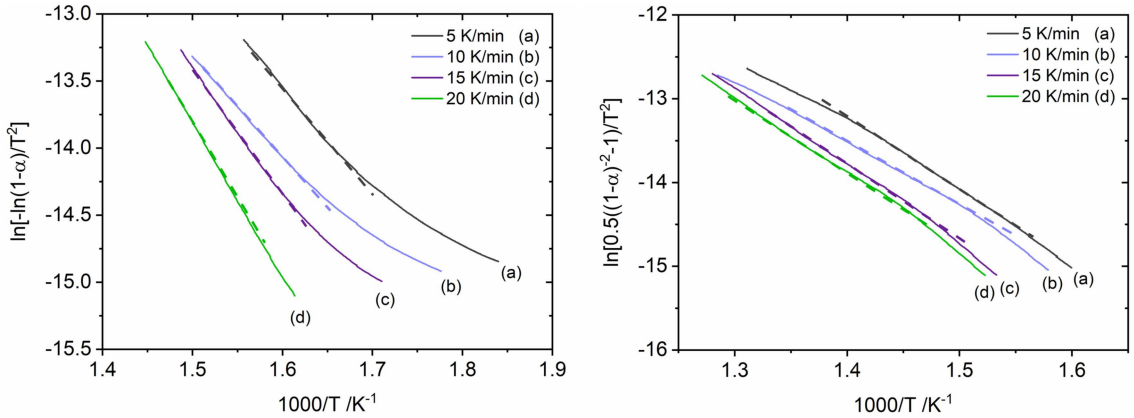

Figure 10. Linear ranges of reduction degree α curves using the F1 solid-state reaction model for sample 2.5 wt% Fe_Citrate_Th (left, straight lines) and those using the F3 solid-state reaction model for sample 7.2 wt% Fe_Nitrate_Th (right, straight lines). Reduction was conducted in 5% H_2 in argon. Dashed lines: Linear regressions. Linear fitting ranges were determined by investigating the effect of extending the fitting borders on corresponding standard derivation. Hence, maximal linear ranges coinciding with good standard derivations were considered.

$$ln\left(\frac{g(\alpha)}{T^2}\right) = ln\left(\frac{AR}{\beta E_a}\left[1-\left(\frac{2RT}{E_a}\right)\right]\right) - \frac{E_a}{RT}, \quad (3)$$

with integral solid-state reaction model $g(\alpha)$, temperature T, heating rate β, apparent activation energy of rate-determining step E_a, gas constant R, and pre-exponential (frequency) factor A.[34,35] Only for suitable solid-state reaction models, depicting $ln[g(\alpha)/T^2]$ as function of reciprocal temperature yields straight lines. Apparent activation energies can be obtained from the slope of resulting straight lines.[34,35] Only solid-state reaction models, $g(\alpha)$, resulting in similar apparent activation energies as obtained from model-independent Kissinger method as well as good linear regressions were selected for further analysis.

For all citrate_Th samples, F1, D2, A3, and R2 solid-state reaction models revealed wide linear ranges by plotting $ln[g(\alpha)/T^2]$ as function of reciprocal temperature. Linear ranges of reduction degree α curves using the F1 solid-state reaction model for 2.5 wt% Fe_Citrate_Th are depicted in Figure 10, left. As observed for 2.5 wt% Fe_Citrate,[17] apparent activation energies at different heating rates for diffusion and Avrami-Erofeyev reaction models, i.e. D2 and A3 reaction models, were significantly higher or lower compared to the results of Kissinger method. Hence, neither the D2 nor the A3 solid-state reaction model were considered for further analysis. The R2 reaction model is denoted geometrical contraction model. For reactions described by the R2 model, nucleation occurs on the surface of the cylindrical crystal and the decreasing interface area between reactant and product phase during reaction determines the reaction rate.[34] This concept appeared hardly applicable to citrate_Th samples with small and dispersed iron oxidic species located in the pore system of SBA-15. For the F1 solid-state reaction model, not only values of apparent activation energy agreed with those obtained from Kissinger method, but also underlying concept was well applicable to small and dispersed iron oxidic species of citrate_Th samples. Consequently, the F1, Mampel, model was chosen as suitable solid-state reaction model for 2.5 wt% Fe_Citrate_Th and all other citrate_Th samples. For citrate samples, thick layer calcination did not lead to a change in suitable solid-state reaction model.

For lowest loaded nitrate_Th sample, analysis procedure according to Coats-Redfern method also resulted in F1 solid-state reaction model being suitable for describing the reduction. Hence, thick layer calcination of 2.0 wt% Fe_Nitrate induced no change in suitable solid-state reaction model.[17]

Here, assuming order-based reaction models as suitable reaction models seemed reasonable regarding the underlying assumptions of these reaction models. Order-based reaction models are considered as the simplest solid-state reaction models. Furthermore, these reaction models are similar to those used in homogeneous kinetics.[17,34,36] For homogeneous kinetics, weakly interacting ions in solution are described. There, the reaction rate of order-based reaction models is proportional to the concentration of active sites. Solid-state reactions described by a first-order model start with a large number of nucleation sites resulting in fast nucleation. Similar to Fe_xO_y/SBA-15 samples calcined in thin layers,[17] reduction of citrate_Th samples and lowest loaded nitrate_Th sample was described by a first-order reaction model. Thus, reduction of these samples was neither inhibited by an increasing product layer nor by limited mobility of reactants. Despite an increased iron species size obtained by thick layer calcination compared to thin layer calcination, Fe^{III} species of citrate_Th and 2.0 wt% Fe_Nitrate_Th still constituted very small nucleation sites.

Conversely, for higher loaded nitrate_Th samples, F1, D1, R3, and F3 solid-state reaction models revealed wide linear ranges by plotting $ln[g(\alpha)/T^2]$ as function of reciprocal temperature. Linear ranges of reduction degree α curves using the F3 solid-state reaction model for 7.2 wt% Fe_Nitrate_Th are depicted in Figure 10, right. Apparent activation energies for solid-state reaction models F1, D1, R3, and F3 obtained from the slope of resulting straight lines are given in Table 4.

For the D1 solid-state reaction model, apparent activation energies of reduction at different heating rates were significantly higher compared to the result from Kissinger method.

Table 4. Apparent activation energy, E_a, of reduction of 7.2 wt% Fe_Nitrate_Th depending on the applied solid-state reaction model.[a]

Heating rate/ K min^{-1}	E_a/kJ mol^{-1} D1	R3	F1	F3
5	122.4 ± 0.3	59.1 ± 0.2	58.8 ± 0.1	74.2 ± 0.1
10	135.9 ± 0.6	66.7 ± 0.3	58.6 ± 0.4	68.5 ± 0.2
15	141.0 ± 0.8	69.0 ± 0.4	64.7 ± 0.3	77.2 ± 0.2
20	144.2 ± 0.9	74.6 ± 0.3	59.1 ± 0.3	75.8 ± 0.2

[a] Reduction was conducted in 5% H_2 in argon at various heating rates.

Consequently, the D1 was not further considered as suitable reaction model for the reduction of 7.2 wt% Fe_Nitrate_Th. Moreover, the F1 solid-state reaction model yielded significantly lower values of apparent activation energy compared to that resulted from model-independent solid-state kinetic analysis method. This indicated that thick layer calcination of 7.2 wt% Fe_Nitrate induced a change in suitable solid-state reaction model. Therefore, first-order reaction model, F1, was no longer suitable for describing the reduction of 7.2 wt% Fe_Nitrate_Th. Apparent activation energies which resulted from the R3 reaction model were also lower than that from Kissinger method. Besides lower values of apparent activation energy, R3 reaction model appeared hardly applicable to the reduction of 7.2 wt% Fe_Nitrate_Th regarding the underlying assumptions of this reaction model. The R3 reaction model is described as contracting sphere model. Accordingly, nucleation occurs rapidly on the surface of the particles. Geometrical contraction models (R) assume a reaction interface progressing towards the center of the crystal particle during reaction.[34] However, Fe^{III} species in 7.2 wt% Fe_Nitrate_Th were small and located in the pore system of SBA-15. Only a minor fraction of higher aggregated iron oxidic species and crystalline α-Fe_2O_3 was observed for this sample, excluding the R3 as suitable reaction model. Consequently, third-order, F3, solid-state reaction model was chosen as suitable reaction model for the reduction of 7.2 wt% Fe_Nitrate_Th. Analysis procedure for 9.3 wt% Fe_Nitrate_Th also resulted in F3 reaction model being suitable for describing the reduction mechanism of this sample. The increased reaction order for higher loaded nitrate_Th samples was correlated with an increased amount of higher aggregated iron oxidic species and the presence of a minor fraction of crystalline α-Fe_2O_3 (Figure 4). For the mechanical mixture Fe_2O_3/SBA-15, reaction model R3 was recently shown to be suitable.[17] This was consistent with crystalline α-Fe_2O_3 particles mixed with SBA-15.

2.5. Correlation of Structural and Solid-State Kinetic Properties

Similar to Fe_xO_y/SBA-15 samples obtained from thin layer calcination,[17] results from sample characterization agreed well with those from solid-state kinetic analysis for Fe_xO_y/SBA-15 samples obtained from thick layer calcination. Thick layer calcination induced an increased iron oxidic species size due to an extended retention time of gaseous decomposition products of the precursors during synthesis of Fe_xO_y/SBA-15_Th. Compared to Fe^{III} ions of the citrate precursor, those of the nitrate precursor were less dispersed before calcination. This yielded a more pronounced Fe_xO_y species growth and aggregation for nitrate_Th compared to citrate_Th samples. This increased iron oxidic species size of nitrate_Th samples correlated with lower values of apparent activation energy of reduction for iron loadings higher than 2.5 wt% compared to citrate_Th samples (Table 3). Furthermore, within the nitrate_Th samples, increasing iron oxidic species size and increasing amount of higher aggregated iron oxidic species with increasing iron loading induced a decreasing apparent activation energy of reduction. Besides, increased amount of crystalline α-Fe_2O_3 for 7.2 wt% Fe_Nitrate_Th and 9.3 wt% Fe_Nitrate_Th coincided with values of apparent activation energy in reduction similar to that of the mechanical mixture, Fe_2O_3/SBA-15. Moreover, results from Coats-Redfern method agreed with those from structural characterization. For higher loaded nitrate_Th samples, significantly increased iron oxidic species size correlated with an increased reaction-order of suitable solid-state reaction model (F3).

Compared to nitrate_Th samples, for citrate_Th samples, the influence of powder layer thickness during calcination on structural and solid-state kinetic properties was less pronounced. Despite increased iron oxidic species size due to thick layer calcination, resulting iron oxidic species remained significantly smaller and higher dispersed compared to those obtained from nitrate precursor. Moreover, citrate_Th samples with iron loadings higher than 2.5 wt% showed a more pronounced micropore filling, and therefore, a smoother SBA-15 surface compared to corresponding nitrate_Th samples. This was indicative of stronger interactions between iron oxidic species and SBA-15, which were induced by the more pronounced chelating effect of the citrate precursor during synthesis of Fe_xO_y/SBA-15_Th samples. These stronger interactions between iron oxidic species and SBA-15 coincided with the higher values of apparent activation energy in reduction of citrate_Th samples. Smaller iron oxidic species of citrate_Th compared to nitrate_Th samples yielded first-order, F1, solid-state reaction model being suitable to describe the reduction.

Lowest loaded nitrate_Th sample, 2.0 wt% Fe_Nitrate_Th, consisting of similar iron oxidic species as citrate_Th samples, showed analogous results in solid-state kinetic analysis as citrate_Th samples. Precursor-dependent differences in reducibility and solid-state kinetic properties of Fe_xO_y/SBA-15_Th samples were predominantly correlated with precursor-dependent differences in resulting iron oxidic species size.

Thick layer calcination of lowest loaded samples induced the most distinct increase in iron oxidic species size and broadened species size distribution. This was ascribed to the highest difference in retention time of gaseous decomposition products between thick and thin layer calcination for lowest iron loadings. These differences in structural characteristics were reflected in the significantly increased apparent activation energy in reduction determined by Kissinger method for 2.5 wt% Fe_Citrate_Th and 2.0 wt% Fe_Nitrate_Th.

3. Conclusion

Iron oxidic species supported on silica SBA-15 were synthesized with iron loadings ranging between 2.0 wt% and 10.7 wt% using two different Fe^{III} precursors (Fe^{III} nitrate nonahydrate, (NH_4, Fe^{III}) citrate). Calcination was conducted in either thin (0.3 cm) or thick (1.3 cm) powder layer. Varying powder layer thickness during calcination significantly influenced structural and solid-state kinetic properties of Fe_xO_y/SBA-15 samples. Additionally, the magnitude of the influence of powder layer thickness during calcination was dependent on both Fe^{III} precursor and iron loading. Structural characterization of Fe_xO_y/SBA-15_Th samples confirmed iron oxidic species being successfully located in the pore system of SBA-15. Thick layer calcination induced an enhanced iron oxidic species growth and resulting iron oxidic species were larger compared to those obtained from thin layer calcination. This yielded an increased degree of micropore filling and a smoother SBA-15 surface for iron loadings higher than 2.5 wt%. Precursor-dependent differences in iron oxidic species growth during thick layer calcination were induced by different strengths of chelating effect of the Fe^{III} precursors. Only for nitrate_Th samples with iron loadings higher than 2.0 wt%, significant amounts of higher aggregated Fe_xO_y and small α-Fe_2O_3 particles were observed. For all other Fe_xO_y/SBA-15_Th samples, long-range ordering was excluded. Differences in solid-state kinetic properties of Fe_xO_y/SBA-15 catalysts dependent on powder layer thickness during calcination correlated with differences in iron oxidic species size.

Experimental Section

Sample Preparation

Mesoporous silica SBA-15 was prepared according to Zhao et al.[2] The surfactant, Pluronic® P123, was dissolved in a mixture of deionized water and HCl (37%) and the reaction mixture was stirred at 308 K for 24 h. Tetraethylorthosilicate (TEOS) was added to the solution and the reaction mixture was stirred at 308 K for 24 h. Subsequently, the solution was hydrothermally treated in pressure-resistant bottles at 388 K for 24 h. The product was filtered, washed with a mixture of deionized water and ethanol (20:1), air-dried, and calcined. Calcination was carried out in three steps. (I) 378 K for 135 min, (II) 453 K for 3 h, and (III) 873 K for 5 h. The heating rate was kept at 1 K/min. Iron oxides supported on SBA-15 were prepared by incipient wetness technique. Therefore, an aqueous solution of (NH_4, Fe^{III}) citrate or Fe^{III} nitrate nonahydrate was used.

After drying in air for 24 h, calcination was carried out at 723 K for 2 h in either thin or thick powder layer. In this work, regular calcination mode of Fe_xO_y/SBA-15 samples was thin powder layer calcination, whereby powder layer thickness was 0.3 cm. Conversely, for thick powder layer calcination, powder layer thickness was 1.3 cm. Samples calcined in thick powder layer were denoted with the ending "_Th" to clarify the different powder layer thickness during calcination compared to corresponding Fe_xO_y/SBA-15 samples. Moreover, Fe_xO_y/SBA-15 samples were denoted as citrate or nitrate samples dependent on used precursor. Accordingly, Fe_xO_y/SBA-15 samples calcined in thick powder layer obtained from citrate precursor were denoted citrate_Th samples and those obtained from nitrate precursor nitrate_Th samples. The prepared mechanical mixture of α-Fe_2O_3 and SBA-15 (10.5 wt% Fe) was denoted Fe_2O_3/SBA-15.

After synthesis of Fe_xO_y/SBA-15_Th samples, iron loadings were confirmed by X-ray fluorescence analysis. Furthermore, CHN analysis was performed to confirm a complete decomposition of the precursors. According to the iron loading and the Fe^{III} precursor, samples were denoted 2.5 wt% Fe_Citrate, 6.3 wt% Fe_Citrate, 10.7 wt% Fe_Citrate, 2.0 wt% Fe_Nitrate, 7.2 wt% Fe_Nitrate, and 9.3 wt% Fe_Nitrate.

Sample Characterization

X-Ray Fluorescence Analysis

Quantitative analysis of the metal oxide loadings on SBA-15 was conducted by X-ray fluorescence spectroscopy using an AXIOS X-ray spectrometer (2.4 kW model, PANalytical), equipped with a Rh K_α X-ray source, a gas flow detector, and a scintillation detector. Prior to measurements, samples were mixed with wax (Hoechst wax C micropowder, Merck), ratio 1:1, and pressed into pellets of 13 mm diameter. Quantification was performed by standardless analysis using the software package SuperQ5 (PANalytical).

CHN Elemental Analysis

Elemental contents of C, H, and N were determined using a Thermo FlashEA 1112 Organic Elemental Analyzer (ThermoFisher Scientific) with CHNS–O configuration.

Nitrogen Physisorption

Nitrogen adsorption/desorption isotherms were measured at 77 K using a BELSORP Mini II (BEL Inc. Japan). Prior to measurements, the samples were pre-treated under reduced pressure (10^{-2} kPa) at 368 K for 35 min and kept under the same pressure at 448 K for 15 h (BELPREP II vac).

Powder X-Ray Diffraction

Powder X-ray diffraction patterns were obtained using an X'Pert PRO diffractometer (PANalytical, 40 kV, 40 mA) in theta/theta geometry equipped with a solid-state multi-channel detector (PIXel). Cu K_α radiation was used. Wide-angle diffraction scans were conducted in reflection mode. Small-angle diffraction patterns were measured in transmission mode from 0.4° through 6° 2θ in steps of 0.013° 2θ with a sampling time of 90 s/step.

Diffuse Reflectance UV/Vis Spectroscopy

Diffuse reflectance UV/Vis (DR-UV/Vis) spectroscopy was conducted on a two-beam spectrometer (V-670, Jasco) using a barium sulfate coated integration sphere. (Scan speed 100 nm/min, slit width 5.0 nm (UV/Vis) and 20.0 nm (NIR), and spectral region 220–2000 nm). SBA-15 was used as white standard for all samples.

Temperature-Programmed Reduction

Temperature-programmed reduction (TPR) was performed using a BELCAT_B (BEL Inc. Japan). Samples were placed on silica wool in a silica glass tube reactor. Evolving water was trapped using a molecular sieve (4 Å). Gas mixture consisted of 5% H_2 in 95% Ar

with a total gas flow of 40 ml/min. Heating rates used were 5, 10, 15, and 20 K/min to 1223 K. A constant initial sample weight of 0.03 g was used and H_2 consumption was continuously monitored by a thermal conductivity detector.

Acknowledgements

The authors are grateful to J. Krone for CHN elemental analysis and to S. Schwarz for assistance during N_2 physisorption measurements.

Conflict of Interest

The authors declare no conflict of interest.

Keywords: Fe^{III} precursors · Kinetics · Particle size · Powder layer thickness · Reduction

[1] J. Scholz, A. Walter, T. Ressler, *J. Catal.* **2014**, *309*, 105–114.
[2] D. Zhao, *Science* **1998**, *279*, 548–552.
[3] L. A. Cano, M. V. Cagnoli, N. A. Fellenz, J. F. Bengoa, N. G. Gallegos, A. M. Alvarez, S. G. Marchetti, *Appl. Catal. A* **2010**, *379*, 105–110.
[4] M. Oschatz, W. S. Lamme, J. Xie, A. I. Dugulan, K. P. de Jong, *ChemCatChem* **2016**, *8*, 2846–2852.
[5] H. Huwe, M. Fröba, *Carbon* **2007**, *45*, 304–314.
[6] H. M. Torres Galvis, A. C. J. Koeken, J. H. Bitter, T. Davidian, M. Ruitenbeek, A. I. Dugulan, K. P. de Jong, *Catal. Today* **2013**, *215*, 95–102.
[7] A. S. Al-Fatesh, A. H. Fakeeha, A. A. Ibrahim, W. U. Khan, H. Atia, R. Eckelt, B. Chowdhury, *J. Chin. Chem. Soc.* **2016**, *63*, 205–212.
[8] J. L. G. Fierro, *Metal Oxides: Chemistry and Applications*, Taylor & Francis Group, **2010**.
[9] B. M. Weckhuysen, D. E. Keller, *Catal. Today* **2003**, *78*, 25–46.
[10] I. E. Wachs, *Catal. Today* **1996**, *27*, 437–455.
[11] J. Hagen, *Industrial catalysis. A practical approach*, Wiley-VCH, Weinheim, **2006**.
[12] Z. Gabelica, A. Charmot, R. Vataj, R. Soulimane, J. Barrault, S. Valange, *J. Therm. Anal. Calorim.* **2009**, *95*, 445–454.
[13] K. Cheng, V. V. Ordomsky, M. Virginie, B. Legras, P. A. Chernavskii, V. O. Kazak, C. Cordier, S. Paul, Y. Wang, A. Y. Khodakov, *Appl. Catal. A* **2014**, *488*, 66–77.
[14] J. He, Y. Li, D. An, Q. Zhang, Y. Wang, *J. Nat. Gas Chem.* **2009**, *18*, 288–294.
[15] F. Arena, G. Gatti, G. Martra, S. Coluccia, L. Stievano, L. Spadaro, P. Famulari, A. Parmaliana, *J. Catal.* **2005**, *231*, 365–380.
[16] T. Tsoncheva, J. Rosenholm, M. Linden, L. Ivanova, C. Minchev, *Appl. Catal. A* **2007**, *318*, 234–243.
[17] N. S. Genz, D. Baabe, T. Ressler, *J. Anal. Methods Chem.* **2017**, *2017*, 1–13.
[18] G. Koch, L. Schmack, T. Ressler, *ChemistrySelect* **2016**, *1*, 2040–2049.
[19] Y. Jiang, K. Lin, Y. Zhang, J. Liu, G. Li, J. Sun, X. Xu, *Appl. Catal. A* **2012**, *445–446*, 172–179.
[20] Y. Sun, S. Walspurger, J.-P. Tessonnier, B. Louis, J. Sommer, *Appl. Catal. A* **2006**, *300*, 1–7.
[21] a) A. Khawam, D. R. Flanagan, *J. Pharm. Sci.* **2006**, *95*, 472–498; b) S. Vyazovkin, C. A. Wight, *Annu. Rev. Phys. Chem.* **1997**, *48*, 125–149; c) A. Khawam, D. R. Flanagan, *Thermochim. Acta* **2005**, *429*, 93–102; d) S. Vyazovkin, *Int. Rev. Phys. Chem.* **2000**, *19*, 45–60.
[22] Q. Zhang, Y. Li, D. An, Y. Wang, *Appl. Catal. A* **2009**, *356*, 103–111.
[23] K. S. W. Sing, *Pure Appl. Chem.* **1985**, *57*.
[24] E. P. Barrett, L. G. Joyner, P. P. Halenda, *J. Am. Chem. Soc.* **1951**, *73*, 373–380.
[25] S. Brunauer, P. H. Emmett, E. Teller, *J. Am. Chem. Soc.* **1938**, *60*, 309–319.
[26] M. A. Smith, R. F. Lobo, *Microporous Mesoporous Mater.* **2010**, *131*, 204–209.
[27] P. Pfeifer, *Phys. Rev. Lett.* **1989**, *62*, 1997–2000.
[28] a) M. Kruk, M. Jaroniec, C. H. Ko, R. Ryoo, *Chem. Mater.* **2000**, *12*, 1961–1968; b) C.-M. Yang, B. Zibrowius, W. Schmidt, F. Schüth, *Chem. Mater.* **2004**, *16*, 2918–2925.
[29] R. S. Weber, *J. Catal.* **1995**, *151*, 470–474.
[30] Y. Wang, W. Yang, L. Yang, X. Wang, Q. Zhang, *Catal. Today* **2006**, *117*, 156–162.
[31] N. S. Genz, *Masterarbeit*, Technische Universität Berlin, Berlin, **2015**.
[32] O. J. Wimmers, P. Arnoldy, J. A. Moulijn, *J. Phys. Chem.* **1986**, *90*, 1331–1337.
[33] H. E. Kissinger, *Anal. Chem.* **1957**, *29*, 1702–1706.
[34] A. Khawam, D. R. Flanagan, *J. Phys. Chem. B* **2006**, *110*, 17315–17328.
[35] A. W. Coats, J. P. Redfern, *Nature* **1964**, *201*, 68–69.
[36] A. J. Smith, L. O. Garciano, T. Tran, M. S. Wainwright, *Ind. Eng. Chem. Res.* **2008**, *47*, 1409–1415.

Manuscript received: July 19, 2019
Revised manuscript received: August 22, 2019